Deformation and stress in hydrothermal regions: The case of a disk-shaped inclusion in a half-space

Deformation and stress in hydrothermal regions: the case of a disk-shaped inclusion in a half-space

Lorenzo Mantiloni[a,b], Massimo Nespoli[a], Maria Elina Belardinelli[a], Maurizio Bonafede[a]

[a] *Department of Physics and Astronomy, Alma Mater Studiorum, University of Bologna, Bologna, Italy*
[b] *GFZ German Research Centre for Geosciences, Potsdam, Germany*

Abstract

Hydrothermal regions are affected by a wide variety of phenomena, including ground inflation and deflation episodes. Among them, calderas offer the opportunity to study the complex interactions between magmatic processes at depth and permeable rocks saturated with fluids in the upper sedimentary layers. One of such regions is the Campi Flegrei caldera in southern Italy, where several source models have been applied over the years to reproduce the ground displacement and seismicity observed during the most recent phase of major unrest (1982-1984). The present work aims at introducing a new source model consisting of a thermo-poro-elastic inclusion embedded in a homogeneous poroelastic half-space. The inclusion is meant to represent a permeable rock layer stressed and strained by hot and pressurized volatiles released upward by an underlying magmatic reservoir and is modeled as a thin horizontal disk inside which a sudden change of temperature and pore pressure occurs. We provide semi-analytical solutions for the displacement and stress fields both within and outside the source and check them by comparison with those obtained through a fully numerical approach. Results provided by our model are compared with two other deformation source models often used to describe volcanic environments in terms of pressurized cavities describing a spherical magma chamber (Mogi source) or a sill-like magma intrusion (Fialko source). For the Campi Flegrei 1982-84 unrest, our model provides a better reproduction of ground deformation data and manages to explain the widespread presence of compressive focal mechanisms, since the stress field promoted both inside and outside the thermo-poro-elastic inclusion is very different from pressurized cavities.

Keywords: Campi Flegrei, Thermo-poro-elasticity, Focal mechanisms, Deformation sources, Volcanism.

1. Introduction

Hydrothermal regions are found in many areas of the Earth, and are in some cases associated with calderas. They are affected by complex interactions in which convection of water and other fluids of magmatic origin within the Earth's crust transfer heat and mass towards the surface. This leads to a variety of observable phenomena, including ground deformation , gravity changes, hot springs, fumaroles and seismicity (see e.g. the Yellowstone caldera, USA, Tizzani et al., 2015; the Rabaul caldera, Papua New Guinea, Robertson and Kilburn, 2016; the Masaya complex, Nicaragua, Williams-Jones et al., 2003; the Long Valley caldera, USA, Hill, 2006; Prejean et al., 2002; Sorey et al., 1991; the Hengill volcanic system, Iceland, Feigl et al., 2000). According to physical models, these effects are generally connected with hydrothermal processes (Rinaldi et al., 2010, Todesco et al., 2014), involving temperature and pore-pressure changes of fluids flowing through permeable rocks, but also with the inflation or deflation of the parent magma chamber related to the mass input/output, to internal differentiation processes or to the emplacement of a new magmatic body (Macedonio et al., 2014; Di Vito et al., 2016). In particular Lima et al. (2009) consider ground deformation episodes as due to the cooling and crystallization of a magma volume at shallow depth, accompanied by release of magmatic fluids which are occasionally expelled from a deep, pressurized, region into the shallow hydrothermal system. In the Lima et al. (2009) conceptual model, subsidence could result from a volume decrease due to both crystallization and a decrease in the flux of magmatic fluids entering the system, or a rapid permeability increase (and pore pressure decrease) that occurs when the fluid pressure exceeds the local strength of the crust, leading to failures in the elastic matrix of the porous media. As the discrimination between these processes is not trivial, the modelling of these phenomena is most important to improve the comprehension of volcanic hazard.

Ground deformation in volcanic areas is usually modeled in terms of the surface effects of a deformation source at depth, typically consisting of a pressurized cavity representing a magma chamber (e.g. Mogi, 1958, Yang et al., 1988) or a horizontal circular crack, suited to model sill-like magma intrusions (e.g. Fialko et al., 2001). Such models assume the source to be embedded in a homogeneous, elastic half-space and neglect the presence of fluids within the rocks. In the present paper we consider the mechanical effects induced by temperature and pore-pressure changes within a thermo-poro-elastic inclusion sourrounded by an elastic medium. Conceptually similar thermo-poro-elastic models were employed to study the effects of pressure

and temperature gradients around wellbores, accounting for deformation sources with cylindrical geometries located within unbounded media (e.g. Myklestad, 1942; Perkins et al., 1984 and Perkins et al., 1985). To model subduction above gas or oil reservoirs, Geertsma et al. (1973) considered the effect of a drop in pore pressure within a finite cylindrical volume in an elastic half-space, retrieving analytical solutions for surface displacement components. Myklestad (1942) developed anaytical solutions for stress components close to a semi-infinite circular cylinder inside which a uniform increase of temperature occurs.

In the present work we introduce a deformation source consisting of a disk-shaped horizontal Thermo-Poro-Elastic (TPE) inclusion embedded in a poro-elastic half space in free drainage conditions. As in Belardinelli et al. (2019) the TPE inclusion is meant as a region of permeable rock being affected by a sudden increase in temperature and pore pressure, embedded in a surrounding medium in isothermal drained conditions. It is worth to notice that purely magmatic models hardly explain long-lasting subsidence (Calò and Tramelli, 2018 and Troise et al., 2018) and are not suitable for the shallow source regions where the presence of large magma bodies can be ruled out. Moreover, differently from a pressurized cavity, the TPE model provides a strong deviatoric stress field even within the source. Belardinelli et al. (2019) consider a spherical shell-shaped TPE inclusion surrounding a fluid filled magma chamber and embedded within an unbounded poro-elastic medium; in the present work we (i) include the free surface boundary condition and (ii) consider a disk-shaped TPE inclusion. Including the free surface is fundamental in order to compare model predictions with observed fault mechanisms above the magma reservoir and with surface displacement. With respect to a spherical shell surrounding the magmatic intrusion, a disk-shaped region is better suited to describe a horizontal permeable rock layer stressed and strained by hot and pressurized volatiles. For example, at Campi Flegrei at about 2 km depth, there is evidence of a seismic layer separating a deeper magmatic body from the shallower acquifer (Figure 8 in Calò and Tramelli, 2018), the most permeable part of which may allow the magmatic fluids to flow upward.

In the next sections we present the semi-analytical formulation of the model. As the present model is inspired by observations made in the Campi Flegrei caldera in southern Italy (fig. 1), in the last section we provide an application focused on one of its unrest episodes. During the period 1982-84 the recorded uplift at Campi Flegrei was nearly axi-symmetric and centered in the town of Pozzuoli (Bonafede and Ferrari, 2009) where it reached its maximum with rate values up to 1 m/yr. One of the most relevant aspects of the 1982-84 unrest was the important increase in seismic activity, while the previous episodes of uplift were

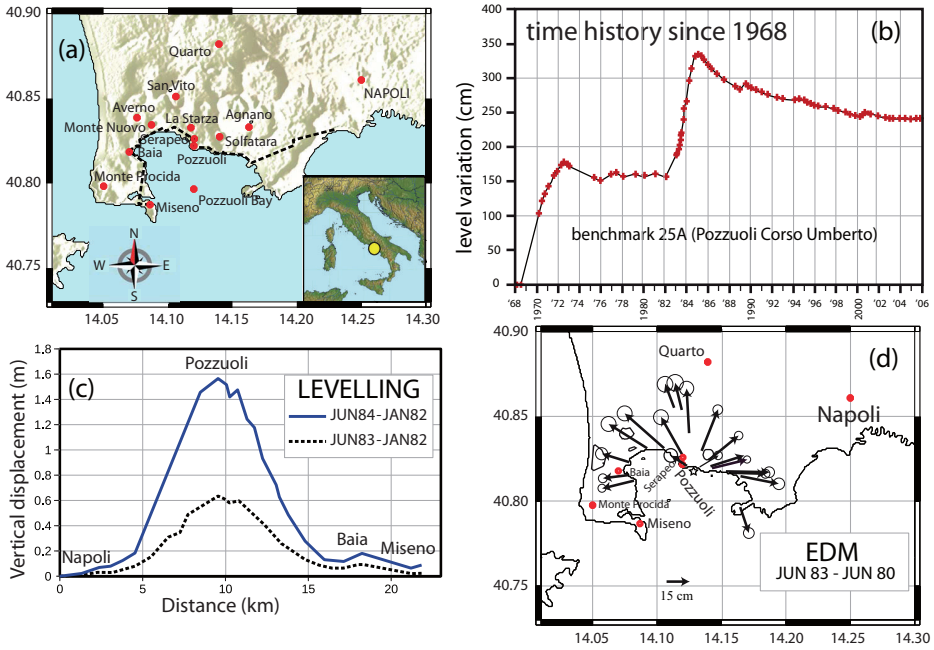

Figure 1: Map and deformation data of the studied area. a) Map of the Campi Flegrei region. b) evolution of uplift at benchmark 25A (Pozzuoli Corso Umberto) since 1968 to 2006. c) pattern of uplift measured on the baseline between Napoli and Miseno (drawn in a) as a dashed black line) in June 1983 (black dotted line) and in June 1984 (blue) with respect to January 1982; the maximum uplift was close to the center of Pozzuoli. d) displacement vectors estimated from EDM (Electromagnetic Distance Measurement) from Jun 80 to Jun 83 referred to the point shown as a star (Amoruso et al., 2014). White circles represent errors.

accompanied by weak to moderate seismicity (D'Auria et al., 2014). The contribution of both magmatic intrusions and hydrothermal dynamics to surface ground deformation was envisaged for this episode (e.g. Belardinelli et al., 2019). Our results will be compared with some of the principal source models used for the 1982-84 unrest, in particular attention is paid to inversion of surface deformation data and the expected distributions of focal mechanisms versus related evidences.

It is worth to notice that, despite having been inspired by the features of one particular case of study, the simple geometry and characteristics of our model make it applicable to the study of other hydrothermal regions around the world.

2. Methods

Following Eshelby (1957) we retrieve the displacement and stress fields associated to the TPE inclusion. The procedure has already been outlined in details by Belardinelli et al. (2019). The strain field e_{ij} of a thermo-poro-elastic medium (McTigue, 1986) undergoing changes of stress τ_{ij}, temperature ΔT and pore pressure Δp is

$$e_{ij} = \frac{1}{2\mu}\left(\tau_{ij} - \frac{\nu}{1+\nu}\tau_{kk}\delta_{ij}\right) + \frac{1}{3H}\Delta p\delta_{ij} + \frac{1}{3}\alpha\Delta T\delta_{ij} \quad (1)$$

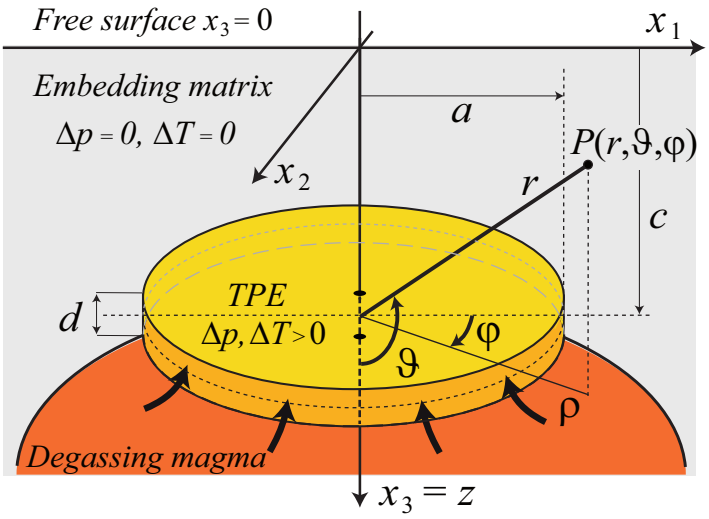

Figure 2: Schematic picture of the disk-shaped thermo-poro-elastic inclusion. The inclusion (yellow region) has a radius a and thickness d; it is located at depth c and embedded in a poro-elastic half-space (grey region). The inclusion undergoes a sudden change in temperature ΔT and pore pressure Δp caused by degassing of a underlying magma body (orange region). The median plane of the disk is drawn with a dotted line. The spherical and cylindrical coordinates (r, θ, φ) and (ρ, φ, z), respectively, are expressed in a reference frame with origin in $x_1 = 0, x_2 = 0, x_3 = c$.

while the inverse relation is

$$\tau_{ij} = 2\mu e_{ij} + \lambda e_{kk}\delta_{ij} - K\left(\frac{1}{H}\Delta p\delta_{ij} + \alpha\Delta T\delta_{ij}\right) \tag{2}$$

where H is the Biot's constant, α the coefficient of thermal expansion , μ the rigidity, ν the drained isothermal Poisson's ratio and $K = \frac{2\mu(1+\nu)}{3(1-2\nu)} = \lambda + \frac{2}{3}\mu$ the drained isothermal bulk modulus of the poroelastic medium. Following eq. (1), the stress-free strain e^*_{ij} that the inclusion would undergo in absence of the hosting medium (Belardinelli et al., 2019) can be expressed as:

$$e^*_{ij} = e_0\delta_{ij} \quad \text{where} \quad e_0 = \frac{1}{3H}\Delta p + \frac{1}{3}\alpha\Delta T \tag{3}$$

Surface tractions $T_k = -3Ke_0n_k$ must be applied in isothermal and drained conditions to restore the original volume and shape of the inclusion. Outside the inclusion the tractions vanish, so that a traction discontinuity $[T_k]^+_- = 3Ke_0n_k$ appears on the TPE inclusion boundary S. When removing the traction discontinuity across S, the following displacement is produced (see e.g. Aki Richards, p. 58)

$$u_i(\mathbf{x}) = \oint_S G_{ik}(\mathbf{x},\mathbf{x}')\,[T_k]^+_-\,dS' = 3Ke_0\oint_S G_{ik}(\mathbf{x},\mathbf{x}')n_k(\mathbf{x}')dS' \tag{4}$$

where G_{ik} is the elastic Green's tensor for a half-space with drained, isothermal elastic parameters, whose components are given by Mindlin (1936). The Green's function $G_{ik}(\mathbf{x},\mathbf{x}')$ yields the displacement in the

$i-th$ direction at point $\mathbf{x}$ due to a unitary point force acting in the $k-th$ direction at $\mathbf{x}'$. By applying Gauss' theorem we obtain

$$u_i(\mathbf{x}) = 3Ke_0 \int_{V_S} \frac{\partial G_{ik}}{\partial x'_k}(\mathbf{x}, \mathbf{x}')dv(\mathbf{x}') \tag{5}$$

where V_S is the volume of the TPE inclusion. The displacement caused by the TPE source everywhere in the half-space is provided by equation (5). Instead the stress field τ_{ij} caused by the TPE source is provided by eq. (2) and should be defined separately within the inclusion, where $\tau_{ij} = \tau_{ij}^{in}$, and outside it, where $\Delta p = 0$, $\Delta T = 0$ and $\tau_{ij} = \tau_{ij}^{out}$, so that

$$\tau_{ij}^{in} = \lambda e_{kk}\delta_{ij} + 2\mu e_{ij} - 3Ke_0\delta_{ij} \tag{6a}$$

$$\tau_{ij}^{out} = \lambda e_{kk}\delta_{ij} + 2\mu e_{ij} \tag{6b}$$

with $e_{ij} = \frac{1}{2}\left(\frac{\partial u_i}{\partial x_j} + \frac{\partial u_j}{\partial x_i}\right)$. Since $G_{ik}(\mathbf{x}, \mathbf{x}')$ is singular, when $\mathbf{x} \to \mathbf{x}'$ particular care must be taken when computing u_i, e_{ij} and τ_{ij} within the inclusion.

2.1. Retrieval of the displacement field: singular and non-singular terms

The three components of the displacement field u_i are found by first evaluating the sum of Green's tensor partial derivatives in eq. (5), employing cartesian coordinates. Their expressions can be written as

$$\begin{aligned}
u_1 &= 3KCe_0 \int_{-a}^{a} dx'_1 \int_{-f(x'_1)}^{f(x'_1)} dx'_2 \int_{c-\frac{d}{2}}^{c+\frac{d}{2}} dx'_3 \; (x_1 - x'_1)\left\{\frac{1}{R_1^3} + \frac{(3-4\nu)}{R_2^3} - \frac{6x_3(x_3+x'_3)}{R_2^5}\right\} \\
u_2 &= 3KCe_0 \int_{-a}^{a} dx'_1 \int_{-f(x'_1)}^{f(x'_1)} dx'_2 \int_{c-\frac{d}{2}}^{c+\frac{d}{2}} dx'_3 \; (x_2 - x'_2)\left\{\frac{1}{R_1^3} + \frac{(3-4\nu)}{R_2^3} - \frac{6x_3(x_3+x'_3)}{R_2^5}\right\} \\
u_3 &= 3KCe_0 \int_{-a}^{a} dx'_1 \int_{-f(x'_1)}^{f(x'_1)} dx'_2 \int_{c-\frac{d}{2}}^{c+\frac{d}{2}} dx'_3 \left\{\frac{(x_3-x'_3)}{R_1^3} - \frac{(3-4\nu)(x_3+x'_3)}{R_2^3} - \frac{6x_3(x_3+x'_3)^2}{R_2^5} + \frac{2x_3}{R_2^3}\right\}
\end{aligned} \tag{7}$$

where

$$R_1 = \sqrt{(x_1 - x_1')^2 + (x_2 - x_2')^2 + (x_3 - x_3')^2} \tag{8a}$$

$$R_2 = \sqrt{(x_1 - x_1')^2 + (x_2 - x_2')^2 + (x_3 + x_3')^2} \tag{8b}$$

$$f(p) = \sqrt{a^2 - p^2}, \quad C = \frac{1 - 2\nu}{8\pi\mu(1-\nu)} \tag{8c}$$

and the intervals of integration are given by the geometry of the TPE inclusion (Figure 2). The integrand functions in eqs. (7) can be divided into two parts: the terms depending on $\frac{1}{R_1^3}$ which diverge within the volume of the inclusion (V_s) and those depending on powers of $\frac{1}{R_2}$ which are bounded within V_s. For this reason, the terms depending on $\frac{1}{R_1^3}$ are referred to as the *singular* terms (apex s), while those depending on powers of $\frac{1}{R_2}$ are referred to as the *non-singular* terms (apex ns).

Accordingly, even the displacement field $\mathbf{u}$ is found by summing up two contributions, as follows:

$$\mathbf{u} = \mathbf{u}^s + \mathbf{u}^{ns} \tag{9}$$

The singular contribution to displacement, $\mathbf{u}^s$, can be written as the gradient of a scalar potential Φ (Belardinelli et al., 2019) so that:

$$\mathbf{u}^s = -\frac{e_1}{4\pi}\nabla\Phi \quad \text{with} \quad \Phi(\mathbf{x}) = \int\limits_{V_S} \frac{1}{R_1} dv(\mathbf{x}') \tag{10}$$

where

$$e_1 = e_0 \frac{1+\nu}{1-\nu} \tag{11}$$

The potential in eq. (10) is formally equivalent to the Coulomb electrostatic potential due to a cylindrical volume V_S of charge density $4\pi\epsilon_0$ (see Jackson, 1999), and therefore the integral can be computed employing an expansion in Legendre polynomials $P_l(x)$ if we make the assumption that the thickness d of the cylinder is much smaller than its radius a ($\frac{d}{a} << 1$)

$$\begin{aligned} \Phi(r,\vartheta) &= 2\pi a d \left[1 - |\cos\vartheta| \frac{r}{a} + \sum_{m=1}^{\infty} c_{2m} P_{2m}(\cos\vartheta) \frac{1}{2m-1} \left(\frac{r}{a}\right)^{2m}\right] \quad \text{if } r < a \\ \Phi(r,\vartheta) &= 2\pi a d \sum_{m=0}^{\infty} c_{2m} P_{2m}(\cos\vartheta) \frac{1}{2m+2} \left(\frac{a}{r}\right)^{2m+1} \quad \text{if } r > a \end{aligned} \tag{12}$$

where $c_{2m} = (-1)^m 4^{-m} (2m)! (m!)^{-2}$ and (r, ϑ, φ) are the spherical coordinates of a point (ϑ is the colatitude measured from the z axis) in a reference frame with origin in the disk center (see Figure 2). When $r \approx a$, the

convergence of the above series is extremely slow, so that analytical continuation may be employed. On the other side, the integrals of the *non-singular* terms in (7) are dealt with by performing analytical integrations and simplifying them into single integrals over one coordinate dx'_i, which are computed numerically, yielding the *non-singular* contribution $\mathbf{u}^{ns}$ to $\mathbf{u}$ (see supplementary material).

2.2. Retrieval of the stress field within and outside the inclusion

The strain tensor $e_{ij} = e^s_{ij} + e^{ns}_{ij}$, can be also separated into a singular part, e^s_{ij}, and a non-singular one, e^{ns}_{ij} related to derivatives of $\mathbf{u}^s$ and $\mathbf{u}^{ns}$, respectively. The singular components e^s_{ij} can be obtained analytically from spatial derivatives of the scalar potential (eq. 12) as follows

$$e^s_{rr} = u^s_{r,r},\ e^s_{\vartheta\vartheta} = r^{-1}(u^s_{\vartheta,\vartheta} + u^s_r),\ e^s_{\varphi\varphi} = (r\sin\vartheta)^{-1}(u^s_{\varphi,\varphi} + u^s_r\sin\vartheta + u^s_\vartheta\cos\vartheta), \tag{13}$$

where the spatial derivative of a scalar field Ψ with respect to the variable x is indicated as $\Psi_{,x}$,

$$e^s_{r\vartheta} = u^s_{\vartheta,r},\ e^s_{r\varphi} = 0,\ e^s_{\vartheta\varphi} = 0. \tag{14}$$

The second members of the last equation are obtained considering that $u^s_{\vartheta,r} = r^{-1}(u^s_{r,\vartheta} - u^s_\vartheta)$, being from (10) $u^s_r = \Phi_{,r}$ and $u^s_\vartheta = r^{-1}\Phi_{,\vartheta}$ and $u^s_\varphi = (r\sin\vartheta)^{-1}\Phi_{,\varphi} = 0$, while u^s_r and u^s_ϑ do not depend on φ. In analogy with Belardinelli et al. (2019), it may be shown that the singular dilation outside the inclusion is $e^s_{kk} = 0$, while inside it we have $e^s_{kk} = e_1$. The non-singular components are retrieved by analytical spatial derivatives of $\mathbf{u}^{ns}$, evaluating the corresponding volume integrals in a semianalytical way as made for $\mathbf{u}^{ns}$ itself (see supplementary material). Then the final expressions for τ^{out}_{ij} and τ^{in}_{ij} are

$$\tau^{out}_{ij} = \lambda e^{ns}_{kk}\delta_{ij} + 2\mu\left(e^s_{ij} + e^{ns}_{ij}\right) \tag{15a}$$

$$\tau^{in}_{ij} = \lambda\left(e_1 + e^{ns}_{kk}\right)\delta_{ij} + 2\mu\left(e^s_{ij} + e^{ns}_{ij}\right) - 3Ke_0\delta_{ij} \tag{15b}$$

In order to test the robustness of our results, and to check the correctness of the numerical integration used in the present work, we compare our semi-analytical solutions to the one obtained through a completely numerical method, which employs a surface distribution of orthogonal forces on the surface of the TPE disk to account for the traction discontinuity on it. In fact, as the Green's function $G_{km}(\mathbf{x}, \mathbf{x'})$ yields the displacement in the $k-th$ direction at point $\mathbf{x}$ due to a point force in the $m-th$ direction at $\mathbf{x'}$, the surface integral in eq. (4) can be seen as the displacement field given by point forces distributed over the surface

S of the inclusion and perpendicular to it. The difference between the results of the semi-analytical and numerical methods for a shallow TPE inclusion with $c/a < 3$ (when non-singular contributions are relevant) for both surface displacement and stress in the plane $x_3 = c$ (the median plane of the TPE disk, Figure S1) are negligible, provided that, in the numerical model, the force distribution over the TPE source boundary is dense enough.

3. THE APPLICATION TO THE 1982-84 CAMPI FLEGREI UNREST

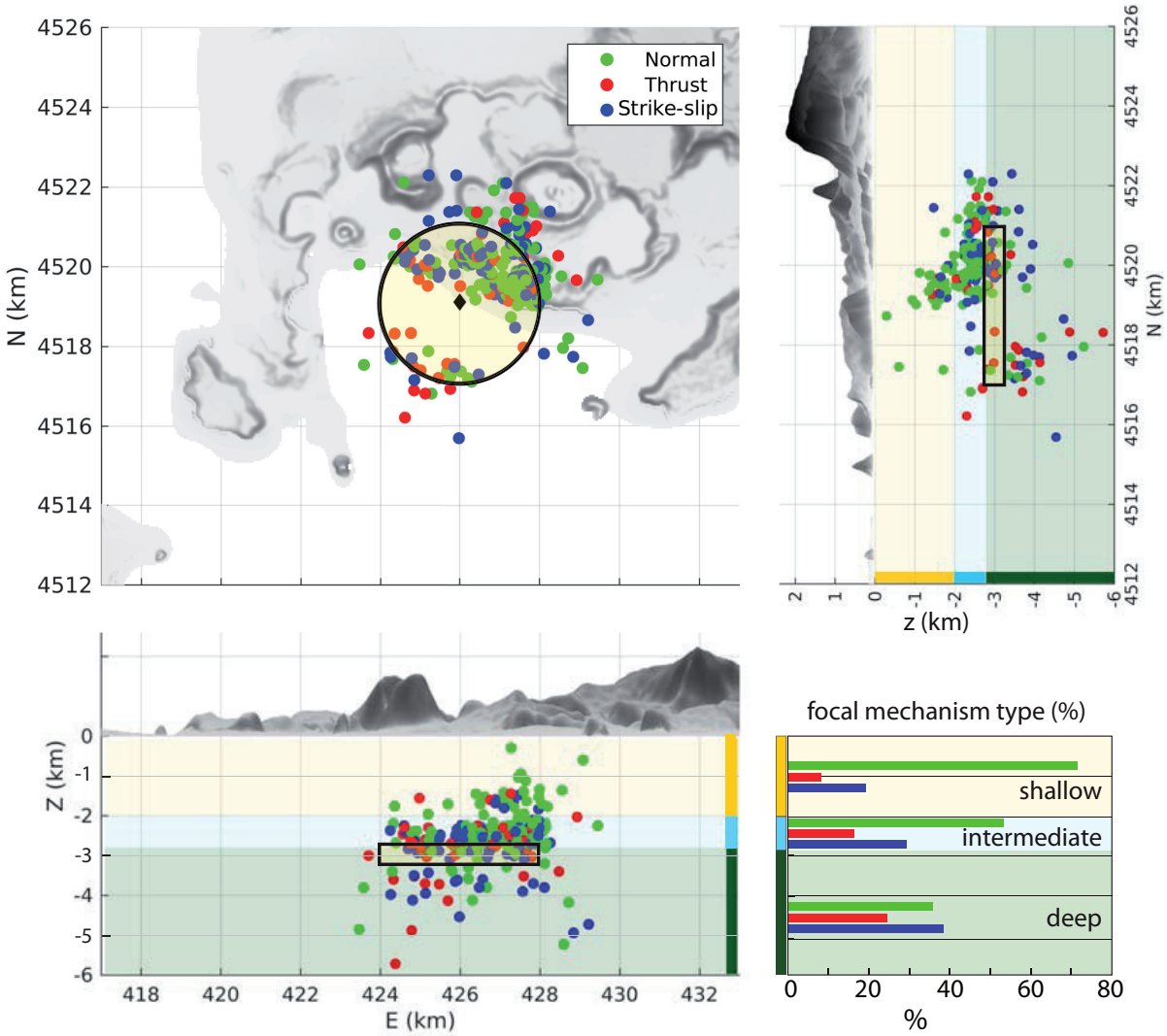

Figure 3: Map and N-S (view from east) and E-W (view from south) vertical sections of the Campi Flegrei Caldera. The topography is vertically exaggerated. Dots represent earthquake locations (D'Auria et al., 2014) occurred during the 1982-84 unrest episode. Normal, thrust and strike-slip mechanisms are associated respectively to green, red and blue colours. The black circle and its projection on the vertical sections represent a tentative location of the TPE inclusion, whose center is shown with a black diamond. Histograms show the percentage of focal mechanism type over the total number of earthquakes located in the relative depth range. The three depth ranges define the shallow (0-2 km, yellow background), intermediate (2-2.8 km, light blue background) and deep (2.8-6 km, dark green background) zone, respectively.

Campi Flegrei is a nested caldera (Figure 1) located west of the city of Naples, with external and internal diameters of about 14 km and 12 km, respectively. Volcanic activity has occurred there since 47,000 years ago (De Vivo, 2006), seeing two major eruptive episodes approximately 39,000 and 14,900 years BP, the last magmatic eruption being that of Monte Nuovo in 1538 AD (Di Vito et al., 2016). In historical times the whole caldera has experienced several cycles of subsidence and uplift (e.g. Di Vito et al., 1999; Di Vito et al., 2016). Two significant phases of uplift recorded by leveling data started in the second half of the 20th century, reaching their peaks in two major unrest episodes in 1969-1972 and 1982-1984 (Figure 1). At the end of 1984 the uplift trend stopped, starting a subsidence phase with a much slower rate which lasted until 2005, when a new period of inflation took over at a slower rate. Both the subsidence and the recent uplift phases were characterized by minor peaks of uplift superimposed on the global trend, which have always been followed by a fast recovery of their whole deformation (Gaeta et al., 2003).

The shape of ground deformation (Figure 1) remained practically unaltered during both up and down movements, maintaining the same features of the 1982-84 episode (Troise et al., 2018). Phases of unrest at Campi Flegrei have been monitored through several techniques over the time, including GPS and InSAR data (Trasatti et al., 2015), seismic (D'Auria et al., 2014) and geochemical data (e.g. Chiodini et al., 2015), gravimetry surveys (Berrino, 1994) and deep drillings (De Natale et al., 2016). Moreover, thanks to the seismic tomography the annular shaped buried rim of the caldera was detected from 800-2000 m to 1800-4000 m of depth beneath which a depressed limestone basement is present at less than 4000 m depth (Zollo et al., 2003, Judenherc and Zollo, 2004). The TPE inclusion is expected within the buried rim of the inner caldera, then in a depth range of 2-4 km as suggested by the tomographic study of Calò and Tramelli (2018). Actually most of geothermal processes (gas emission and boiling pools) are located within few kilometers from the center of the caldera (e.g. Solfatara crater in Figure 1; Chiodini et al., 2015) below which we assume that the TPE source is located (Figure 3).

It is worth to notice that even if the caldera is located in the tectonic environment of the Campania margin, which is characterized by extensional structures and normal fault activity (Lima et al., 2009), the focal mechanisms distribution retrieved from the 1982-84 seismic data series, below the caldera (D'Auria et al., 2014), is very heterogeneous (Figure 3), suggesting a dominant role of local deformation mechanisms related to the volcanic environment. Moreover, the distribution of focal mechanisms is not uniform along depth, as confirmed by the percentage of focal mechanism type computed over the total number of earth-

quakes occurred in the shallow (0-2 km), intermediate (2-2.8 km) and deep (2.8-6 km) zones, respectively (Figure 3). Below the caldera there is a progressive increase of strike-slip mechanisms over depth (from 20 to 39%). The same is true for thrust mechanisms whose percentage changes from about 8 to 25%, while, in contrast, there is a strong decrease in normal mechanisms percentage that reduces from 72 to 36%. The cut-off of the seismicity can be identified at about 4 km depth, even if the hypocenter depth was generally above 3 km (D'Auria et al., 2014).

Different deformation sources have been considered over the years to interpret the cause of the 1982-84 unrest. Berrino et al. (1984) found that the observed bell-shaped pattern of ground uplift can be nicely fitted by a Mogi source located at about 3 km depth beneath the center of the caldera. Battaglia et al. (2006) inverted deformation and gravity data determining pressurized penny-shaped horizontal cracks located in the depth range 2.5 and 3.5 km, probably filled with aqueous fluids, as the probable sources of inflation at Campi Flegrei. Other authors (Amoruso et al., 2008), considering the same source model within a layered embedding medium, support the presence of magma in its interior. More recently, based on considerations about the ratios of the three moment tensor eigenvalues retrieved from the data, Trasatti et al. (2011) concluded that a mixed mode dislocation with both shear and tensile components, through which a magma volume might have intruded, is the most suitable deformation source for the event, ruling out the applicability of a pressurized ellipsoid.

Shallow magmatic intrusions (3-4 km depth) have been advocated as the origin of both the 1982-84 and the 2011-13 unrest episodes (Dvorak and Berrino, 1991; Macedonio et al., 2014). Purely magmatic models, however, fail in explaining the observed long lasting subsidence after the 1982-84 peak (Troise et al., 2018). Moreover, seismic tomography surveys (Judenherc and Zollo, 2004) found no evidence of shallow magma batches in the 3-4 km depth range, while they have highlighted a large sill at about 8 km depth which may feed the entire Neapolitan volcanic area (Zollo et al., 2008). Even the temperature profiles inferred from deep drilling projects (Carlino et al., 2012) are generally incompatible with the presence of magma at shallow depths (Trasatti et al., 2011).

3.1. Choice of parameters

Firstly, we have to define an adequate set of parameters both for the dimensions of the inclusion and the properties of the medium. However we normalize all the TPE inclusion results to $|u_z|^{max}$, the maximum

uplift at the free surface, which realizes on the symmetry axis of the system, and we show patterns using spatial coordinates normalized to the radius of the TPE disk. Accordingly the choice of parameters slightly affects the results shown. The radius of the TPE inclusion and its depth are preliminarly chosen as $a = 2000$ m and $c = 3000$ m as suggested by Battaglia et al. (2006), Amoruso et al. (2008) and D'Auria et al. (2014), employing pressurized horizontal cavities. These parameters are also suggested by the seismicity distribution and the location (between 2 and 4 km) of a shallow V_P/V_S-anomaly possibly related to an overpressurized fluid volume (Chiarabba and Moretti, 2006, Zollo et al., 2008; Calò and Tramelli, 2018). The disk height is chosen so that the ratio $\frac{d}{a} \ll 1$ is suitable to allow the potential expansion in equation (12). For the chosen parameters $|u_z|^{max}$ is in the order of tens of centimeters.

According to Belardinelli et al. (2019), the elastic parameters in isothermal and drained conditions of the poro-elastic matrix are $\lambda = 4$ GPa, $\mu = 6$ GPa ($\nu = 0.2$). The thermal expansion coefficient of the TPE source is $\alpha = 3 \cdot 10^{-5}\mathrm{K}^{-1}$, while $H = 10$ GPa (see eq. 3). These values are pertinent to highly porous sedimentary rocks (Rice and Cleary, 1976), such as those constituting much of the upper stratigraphy of the Campi Flegrei caldera (Lima et al., 2009).

Finally, the changes in temperature and pore pressure within the inclusion are assumed respectively in the order of $\Delta T = 100$ K, $\Delta p = 10$ MPa. The assumption of a 100 K temperature jump is a reasonable order of magnitude if we consider the injection of overheated and overpressurized volatiles from a deep reservoir into a shallower system as sketched in Figure 2. Shallow water reservoirs in the Campi Flegrei area are associated with temperatures between 150° C and 250° C (Carlino et al., 2012), while the critical temperature of water is 373.9° C. An order of magnitude of tens MPa for Δp is well within the difference between the lithostatic and hydrostatic pore pressure at 3 km depth.

4. RESULTS

Given the axial symmetry of the TPE inclusion with respect to the vertical axis z, we provide results using the cylindrical reference frame $(\rho, \varphi, z = x_3)$ shown in Figure 2.

At the free surface, the resulting displacement components are illustrated in Figure 4*a* (solid lines) as functions of ρ/a, where ρ is the horizontal distance from the z axis (see Figure 2). Figure 5*a* and *b* show the components of the stress tensor over the median plane of the TPE inclusion ($x_3 = 3$ km) and slightly above it ($x_3 = 2.5$ km), respectively. In Figure 5*a* inside the TPE inclusion ($\rho < a$), the diagonal stress components

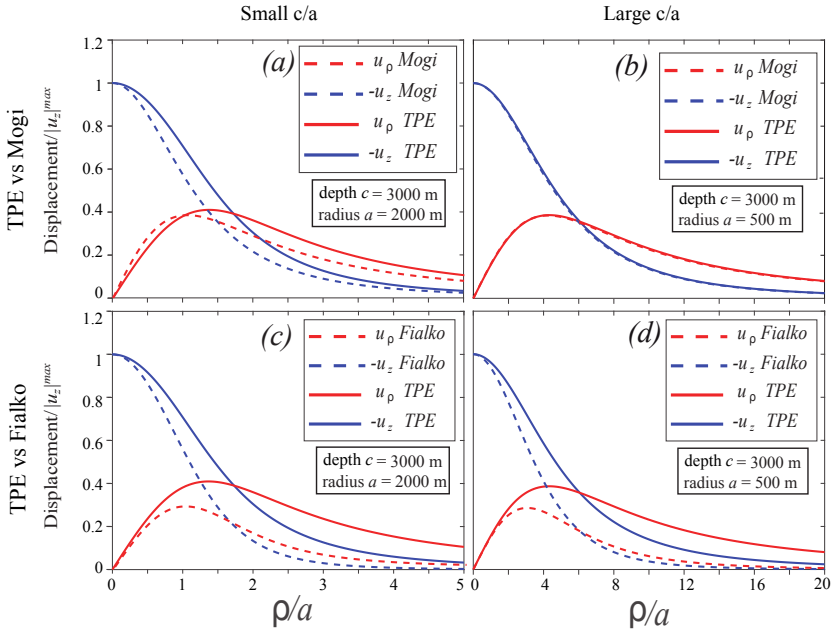

Figure 4: Displacement at the free surface. Comparison between the TPE inclusion and Mogi source (a, b) and TPE inclusion and Fialko source (c, d) of displacement (u_ρ, red lines) and vertical uplift ($-u_z$, blue lines) at free surface. Displacement components are normalized to the maximum value of the vertical uplift for each model ($|u_z|^{max}$). The horizontal distance ρ is normalized to the TPE inclusion radius a. All the source centers are placed in $(0, 0, c)$ with $c = 3000$ m. In panels (a) and (c) we assume a large c/a ratio for the TPE inclusion (a=500 m, $d = 40$ m), in panel (b, d) we assume a small c/a ratio for the TPE inclusion (a=2000 m, $d = 200$ m as used in the present work). The volume of the Mogi source is always assumed as equal to the one of the TPE inclusion, so its radius is 843 m in panel (a) and 196 m in panel (b), while Fialko sources have the same radius as the TPE source. Note the different scales in abscissa.

are almost constant for $\rho < 0.8a$ and $\tau_{zz}^{in} >> \tau_{\rho\rho}^{in} > \tau_{\varphi\varphi}^{in}$ while, outside it ($\rho > a$), $\tau_{zz}^{out} > \tau_{\varphi\varphi}^{out} > \tau_{\rho\rho}^{out}$. Outside the inclusion the stress components rapidly decay with ρ in agreement with the observed cut-off of seismicity getting outside the TPE inclusion boundaries (black circle in Figure 3). All shear components vanish over the median plane. Above the TPE inclusion, the stress strongly decreases and, at a depth of 2.5 km, it is already reduced by two orders of magnitude (Figure 5*b*) even if the decay with ρ is less pronounced than in Figure 5*a*. It is worth to notice that, for $\rho < a$, inside the TPE inclusion (Figure 5*a*), τ_{zz} is the maximum normal stress, while above it (Figure 5*b*), it is the least one. Furthermore, a significant shear component $\tau_{\rho z}$ appears above the inclusion while other shear components $\tau_{\rho\varphi}$ and $\tau_{z\varphi}$ vanish as a consequence of axial symmetry.

Myklestad (1942) addressed the problem of a semi-infinite circular cylinder in an infinite solid inside which a uniform increase in temperature occurs, retrieving analytical solutions for normal and shear stresses both within and outside the source. Notably, both the models predict the same compressive stress regime within the sources, with both $\tau_{\phi\phi}$ and τ_{zz} changing sign from inside to outside the cylinder (compare fig. 5 a with Myklestad, 1942, fig. 2, bottom right). Some differences arise in the normal stress components

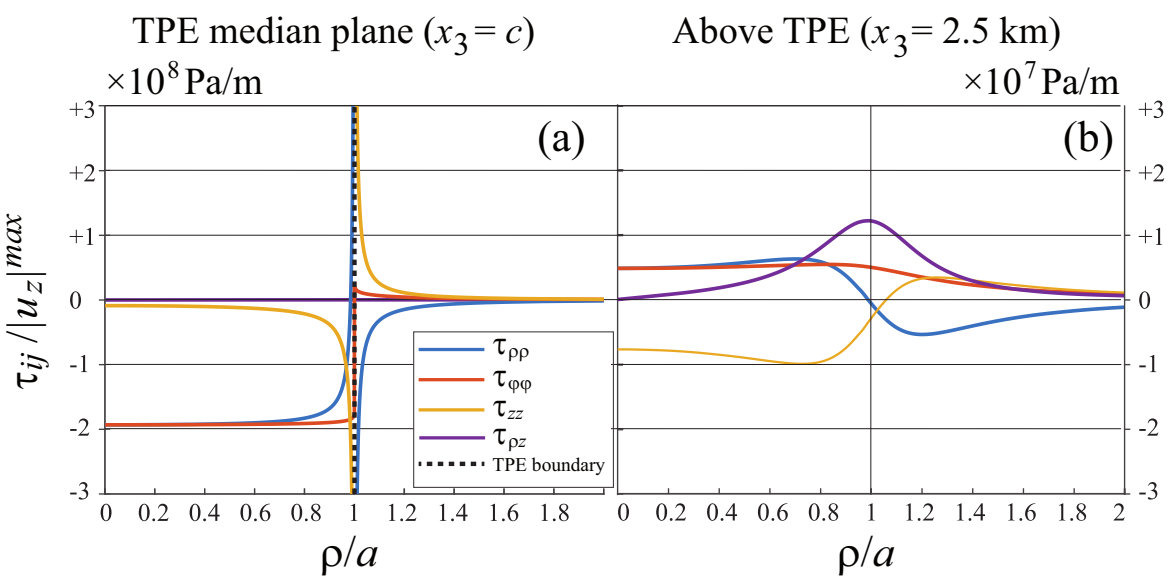

Figure 5: Stress components generated by the TPE disk. a) On the median plane ($z = c = 3$ km) of the TPE inclusion and b) above it ($z = 2.5$ km), stress components τ_{ij} as functions of horizontal distance from the center ρ/a. $|u_z|^{max}$ is the maximum value of vertical uplift. The black dashed line in panel (a) represents the TPE disk boundary $\rho = a$. The TPE disk radius is $a = 2$ km.

calculated on a plane perpendicular to the axis of the cylinder and just below its base (Myklestad, 1942, fig. 2, bottom left) with respect to the ones we retrieved above the TPE disk (fig. 5 b), likely due to the different geometry of the sources and the free surface condition affecting the results of fig. 5 b.

In Figure 4 the TPE disk displacement is compared with results for a point-source approximation of a spherical pressurized source (Mogi, 1958, Figure 4*a* and *b*, dashed lines) and a penny-shaped crack (Fialko et al., 2001, Figure 4*c* and *d*, dashed lines); in the following these sources are simply referred as Mogi and Fialko, respectively. We recall that outside the sperical TPE shell inclusion considered in Belardinelli et al. (2019) for assumed values of e_1, external radius a_2 and internal radius $a_1 < a_2$, (please note the different notation with respect to that paper), results are the same of a Mogi source with the same center, radius $a = a_2$ and overpressure $\Delta P = \frac{4}{3}\mu e_1 \frac{a_2^3 - a_1^3}{a_2^3}$. Accordingly outside the source, $r > a_2$, the Mogi source results are coincident with the ones for the TPE shell inclusion considered in Belardinelli et al. (2019).

In order to compare results for both displacement and stress, we assume the same source depth ($c =$ 3000 m) while the same volume as in the TPE inclusion is assumed for the Mogi source and the same radius ($a =$ 2000 m) for the Fialko source. Results are normalized to $|u_z|^{max}$, the maximum uplift predicted by each model at the surface of the half-space. In this way we can compare the results of the three kinds of sources as if each of them would produce the same (1 m) maximum uplift at free surface, regardless of the

particular choice made for the parameters which affect the displacement linearly.

In Figure 4*b* and *d* the displacement is evaluated assuming for the TPE inclusion a smaller radius a than stated in section 3.1, in order to evaluate the effect of a TPE disk with greater c/a ratio. In the case of the larger c/a ratio, both the radial and the vertical displacement components produced at the free surface by the Mogi source and TPE disk are indistinguishable (Figure 4*b*). As the Mogi source already managed to fit in good approximation the geodetic data at Campi Flegrei (Dvorak and Berrino, 1991), the similarity between these results means that the model we consider cannot be ruled out in the first place in the interpretation of the causes of the uplift. However we shall see that the stress field induced by the TPE disk and the Mogi source are significantly different, in particular within the sources.

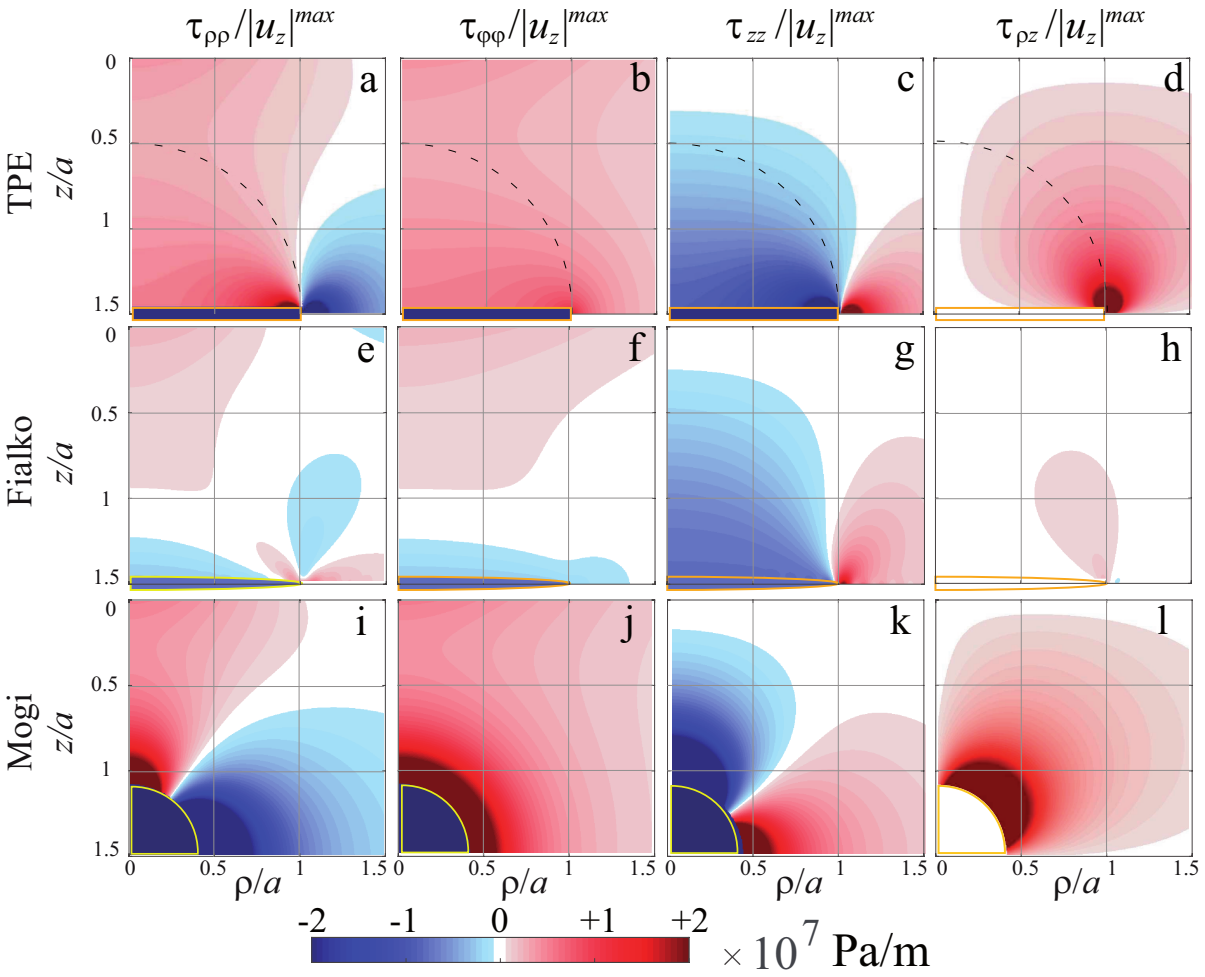

Figure 6: Depth maps of cylindrical stress components. They are plotted over the $\rho - z$ section between the free surface ($\frac{z}{a} = 0$) and the depth of the sources ($\frac{z}{a} = 1.5$). a)-d): cylinder-shaped TPE source; e)-h): Fialko source; i)-l): Mogi source. Stress values of each model are divided by $|u_z|^{max}$, the maximum uplift at the Earth surface predicted by the same model. Horizontal and vertical axes are normalized to the radius a of the TPE inclusion. The singular components of the the TPE disk stresses (obtained from equation 12 are not convergent along the circle $r = a$ (black dashed line in panels a)-d) where the solution should be compared by analytical continuation.

As for the Fialko model (Figure 4*c* and *d*), the displacement components show similar trends, but the maximum horizontal displacement in the case of the TPE source occurs farther from the origin than in the case of the Fialko source, regardless of the c/a ratio. Furthermore, the amplitudes of displacement components computed by TPE inclusion decrease more slowly away from the source than for Fialko. This means that the TPE model may describe situations where the horizontal deformation is not negligible even at considerable distances from the center of the area of maximum uplift, without requiring a greater depth.

Depth maps of the stress components for all the models considered are reported in Figure 6. For the Mogi model, the strain (supplementary material) and stress components were retrieved from the expression for displacement reported by Bonafede and Ferrari (2009) and the constituive relation (2) with $\Delta T = 0$ and $\Delta p = 0$. The stress components of the Fialko model were instead obtained through numerical integration of the analytical expressions published in Fialko et al. (2001): this has been achieved through a modified version of the USGS dMODELS tool (Battaglia, 2017). The stress field of the TPE source (Figure 6*a, b, c* and *d*) differs considerably from the Mogi source (Figure 6*i, j, k* and *l*) and even more from Fialko (Figure 6*e, f, g* and *h*). Similarities may be noted between the τ_{zz} components for the TPE inclusion and Fialko, while only TPE and Mogi sources display a significant $\tau_{\rho z}$ component. It is important to note finally that an extremely high deviatoric stress is present within the TPE source (as shown in Figure 5), while it vanishes within both the Mogi and Fialko sources where an isotropic pressure applies.

The differences between the stress components related to distinct models give rise respectively to a different distribution of expected fault mechanisms on the basis of the Frohlich triangle (Frohlich, 2001). According to this method, the favoured fault mechanisms in each point of the medium is computed by evaluating principal stresses and related axes orientations.

Plots of the expected fault mechanisms and the maximum shear stress on the same vertical section as in Figure 6 are reported for each model in Figure 7. The TPE source is associated with normal faults over an area spanning from the free surface to the upper base of the disk (Figure 2). The lateral extension of this domain reduces progressively with depth, laterally bounded by a region where thrust faults are expected. This pattern is similar to that related to the Mogi source (Figure 7*c*); in particular, both give rise to thrust faults on their median plane, but it is markedly different in the case of the the Fialko source (Figure 7*b*). It is important to note that inside the TPE source, thrust mechanisms are predicted with extremely high deviatoric stress, while the other sources (Mogi and Fialko) are pressurized cavities with internal vanishing

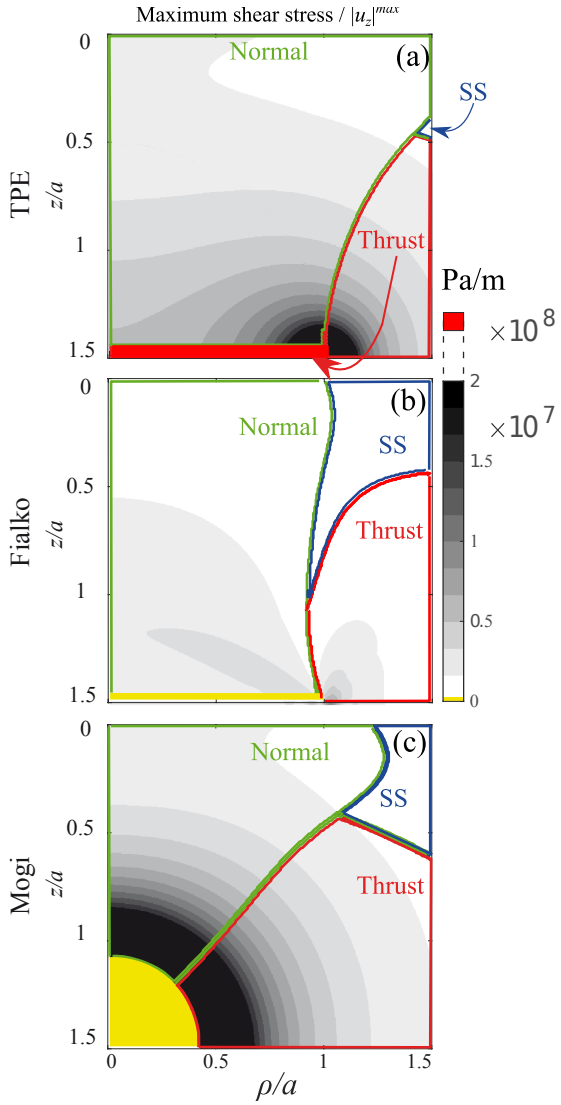

Figure 7: Vertical sections of maximum shear stress. The maximum shear stress (gray coloured palette) is plotted over the $\rho - z$ section between the free surface ($\frac{z}{a} = 0$) and the depth of the sources ($\frac{z}{a} = 1.5$). (a) TPE inclusion, (b) Fialko, (c) Mogi source. Contour includes areas in which each source promotes Normal, Thrust and Strike-Slip (SS) mechanisms. Horizontal and vertical axes are normalized to the radius a of the TPE inclusion. In panels (b) and (c) the internal domain of the sources, where shear stress vanishes, is represented in yellow.

deviatoric stress components.

In order to test the reasonability of parameters of the different models when applied to the Campi Flegrei unrest it is necessary to reproduce the actual deformation field observed during an unrest phase. We considered the data recorded through the EDM tecnique (changes of distance between benchmarks) and the vertical displacement recorded by leveling during the period June 1980 - June 1983 (Figure 1). The maximum uplift was 1.80 m in November 1984 (w.r.t. January 1982), about three times the uplift at the end of the considered observation period (Figure 1*b*). In order to accurately infer model parameter values from inversion of surface data, the hypothesis of a homogeneous medium, common to three different models

Table 1: Results of the inversions and misfits associated to the three models considered. Parameters estimated by inversion of surface data are in bold. TPE-Disk refers to the TPE disk models with fixed aspect ratios $\frac{d}{a} = 0.3$. In the case of the Mogi model the parameter estimated by inversion is $Q = \Delta P \cdot a^3 \frac{1-\nu}{\mu}$, while in the case of the TPE shell $Q = \frac{4}{3} e_0 (1+\nu)(a_2^3 - a_1^3)$, representing the scaling factor for displacement at the surface. We assume $a = a_2 = 0.843$ km as in figures 6-7 and $\frac{a_2 - a_1}{a_2} = 0.3$, being a_1 the internal radius of the TPE shell. Values of ΔP for the Mogi model and e_0 for the TPE-shell are retrieved from the Q value estimated by inversion. Values of the Δp are retrieved from e_0 estimated through inversion assuming $\Delta T = 100$ K. The misfit in the last column refers to the sum of the absolute difference between predicted and observed EDM and leveling.

Model	c (km)	Q (m^3)	ΔP (MPa)	e_0	a (km)	Δp (MPa)	Total misfit (m)
Mogi	**2.7**	**5.121 $\cdot 10^6$**	64.1	–	–	–	3.868
Fialko	**2.9**	–	**3**	–	**2.5**	–	4.678
TPE-DISK	**1.9**	–	–	**1.7 $\cdot 10^{-3}$**	**1.9**	21	2.904
TPE-SHELL	**2.7**	**5.121 $\cdot 10^6$**	–	$8.1 \cdot 10^{-3}$	–	214	3.868

here considered, is inadequate (Trasatti et al., 2011). We are aware of this, but at least for the purpose of model comparison, the inversion of surface data is suitable.

For each model, a direct search in the parameter space was performed using a Monte Carlo sampling. Then the posterior probability density distribution (PPD) of each parameter was estimated by Bayesian inference (*e.g.* Sambridge, 1999). In Table 1 best fit values of parameters allowed free to vary during the inversion are indicated with bold numbers. Other values reported in Table 1 refer to parameters depending on free parameters and the fixed ones. Results for the Mogi source allow us to estimate the parameters of a TPE-shell model (Belardinelli et al., 2019) with the same center, an external radius a_2 and an internal radius a_1 assigned by fixing the ratio $\frac{a_2 - a_1}{a_2} = 0.3$. For the TPE-disk we fixed the geometrical ratio $\frac{d}{a} < 1$ at different values finding that smaller values require shallower and wider disks to reproduce data and the minimum misfit is realized by fixing $\frac{d}{a} = 0.3$. From Table 1 we can see that the TPE-disk provides the minimum mixfit among the three considered models. An Akaike test (e.g. Hurvich and Tsai, 1989) shows that the misfit improvement justifies the increase in the number of parameters.

In Figure 8 we can note that employing best fit values of parameters, the TPE-disk reproduces well both kinds of data, while the Mogi model describes worse leveling data and the Fialko model underestimates EDM data. It is worth to mention that, according to Dieterich and Decker (1975), horizontal data have greater resolving power among different deformation source models.

5. DISCUSSION

We consider a disk-shaped thermo-poro-elastic inclusion embedded in a poro-elastic semi-infinite medium bounded by a free surface (Figure 2) in order to model a sudden input of hot and pressurized fluids from

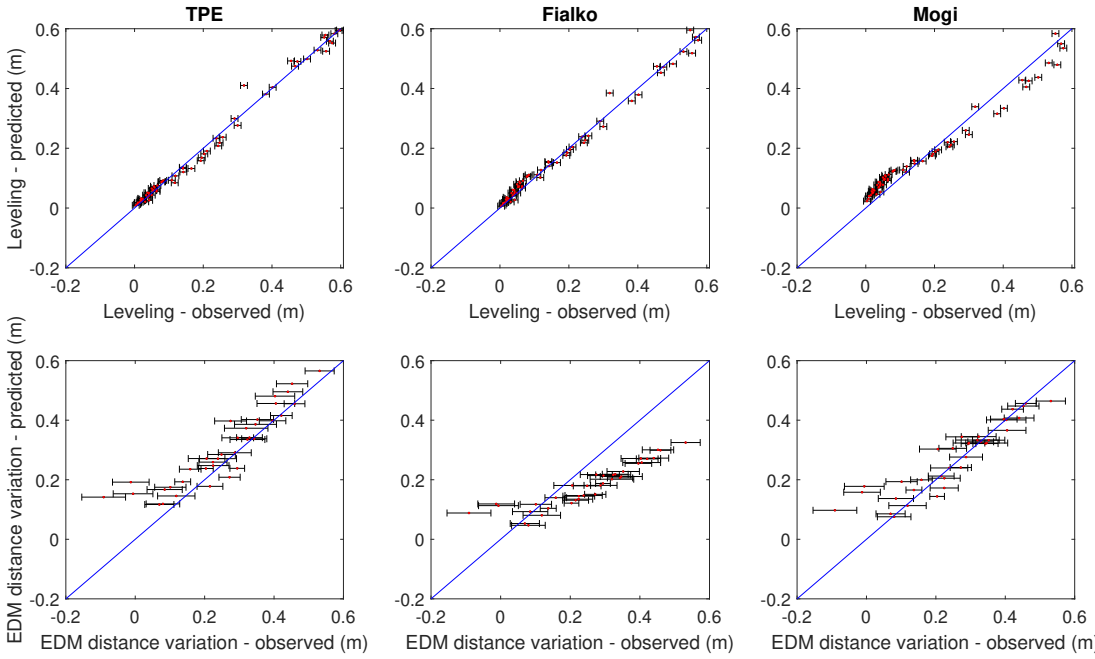

Figure 8: Results of the inversion of levelling (upper row) and EDM (lower row) data of displacement for the period June 1980 and in June 1983 at Campi Flegrei using three different source models (indicated).

an underlying magma body into a permeable region as envisaged by many authors for the Campi Flegrei caldera (e.g. Chiodini et al., 2015; Trasatti et al., 2019, Calò and Tramelli, 2018). Our semi-analytical computations are tested with a fully numerical approach (Figure S1).

The present model is intended to describe surface ground deformation and stress field at depth in hydrothermal regions, and we focus on the 1982-84 unrest episode at Campi Flegrei caldera. The adopted elastic parameters for the external medium and the inclusion represent highly-porous sedimentary rocks which constitute the upper layers of Campi Flegrei stratigraphy.

We compare our results to those of two axially-symmetric source models that have been employed in similar situations: Mogi and Fialko sources. The displacements on the free surface (Figure 4) are in good agreement with those of a Mogi source, in the case of a large c/a ratio, while there are some differences with the Fialko source for both small and large c/a ratio; in that, in our case, the amplitudes of the displacement components decrease more slowly with distance from the source.

All considered sources promote normal fault mechanisms above them (Figure 7) in agreement with data at Campi Flegrei (Figure 3), and thrust mechanisms laterally. A strong deviatoric stress is retrieved within the TPE inclusion (e.g. Figure 5a), unlike Mogi and Fialko sources. The large deviatoric stress inside the

TPE disk is able to promote thrust faults and exceeds by one order of magnitude the values at the same depth outside the source, explaining the increasing percentage of thrust fault mechanisms at increasing depth (Figure 3).

Results of inversion (Table 1) show that in order to obtain 1/3 of the maximum uplift oberved at the surface during the 1982-1984 unrest at Campi Flegrei, the Mogi and Fialko sources require magma overpressures of $\Delta P = 64.1$ and 3 MPa, respectively, for a reasonable value of the radius of the Mogi source, $a = 843$ m, while the TPE-disk requires a pore pressure change of $\Delta p = 21$ MPa, for a temperature change $\Delta T = 100$ K (we recall that according to equation 3, for the same uplift, the requested Δp decreases with increasing ΔT). Following Trasatti et al. (2011), we can assume that to realize the 1.8 m of maximum uplift observed in November 1983, these pressure estimates must be scaled by a factor of 3, leading to unrealistically high magma overpressure values for the Mogi source ($\Delta P \approx 190$ MPa, $Q \approx 1.5 \cdot 10^7$ m^3) with respect to lithostatic values at less than 3 km depth. These parameters are comparable with previous estimates (e.g. Berrino et al., 1984, $Q = 1.3 \cdot 10^7$ m^3, $c = 2.8 \pm 0.2$ km and Bonafede and Ferrari, 2009, $Q = 1.6 \cdot 10^7$ m^3, $c = 3$ km). A previous inversion for the Fialko source (Amoruso et al., 2008), despite considering a different rigidity modulus with respect to the present work, confirms that this kind of source leads to much lower overpressure estimation than that of the Mogi one ($\Delta P = 7$ MPa, $c = 3$ km, $a = 2.7$ km). The same scaling (factor of 3) of the estimates in Table 1 leads, however, to unrealistically high pore pressure changes Δp also in the case of both the TPE-disk and the TPE-shell. Therefore, we can exclude that the big uplift observed during that episode of unrest was totally due to the hydrothermal processes modeled by the TPE source. Instead the present model could be suitable to represent subsequent smaller episodes of uplift ($\sim$ cm) at Campi Flegrei (1989, 1994, 2000 and 2006), that were most likely related to shallow hydrothermal processes (D'Auria et al., 2011). Actually, since 1989 volcanotectonic hypocenters have been confined almost exclusively between 1 and 3 km depth, within the area of most important geothermal output (D'Auria et al., 2011).

The 1982-84 unrest could be likely ascribed to the combined effects of both the emplacement of a magma body at shallow depths and hydrothermal processes. According to Trasatti et al. (2011), the magmatic intrusion can be modeled as due to a dike emplacement in a compressive stress regime region below the center of the caldera, consisting of a tensile dislocation with a reverse-slip component. As the TPE source provides strong compressive stress regime inside, it can give support to the model of Trasatti et al. (2011)

suggesting that during dike emplacement, the latter may have met the TPE source. Furthermore thrust faulting mechanisms are reported by Ekstrom (1994) and Nettles and Ekstrom (1998) in different volcanic regions.

The Fialko model requires smaller ΔP than the Mogi source (Table 1). However, the presence of a large magmatic reservoir at 2.9 km depth (Table 1) seems incompatible with the brittle rheology and with temperatures met during deep drilling in nearby wells (400° C at 3 km depth, e.g. Carlino et al., 2012).With respect to both Fialko and Mogi model , the main advantage of the TPE inclusion is the retrieval of a stress field at different depths with strong differences between the interior and the exterior of the source, which could account for the high heterogeneity of closely located seismic mechanisms observed at Campi Flegrei during the 1982-84 episode. Moreover the TPE source: (i) differently from the Fialko model, can easily explain the increase of the percentage of thrust mechanisms over depth (Figure 3); (ii) compared to the Fialko model for the same maximum uplift at the surface the TPE disk generates much larger shear stresses (Figure 7). The reason is that the crack represented by the Fialko model is very efficient in producing high displacement with low overpressure and then low stresses.

All models fail to produce strike slip faulting apart from shallow far field regions, where in any case the induced shear stress is small (Figure 7). Instead at Campi Flegrei strike-slip faulting is frequent in near field (Figure 3). However, even a small additional component of regional stress may easily exchange the order of τ_{zz} and $\tau_{\rho\rho}$ (Figure 5b), so that strike-slip faulting can be promoted in external regions close to TPE disk.

Both poro-elastic and thermo-elastic effects are considered in our model. Temperature changes are more effective than pore-pressure changes in inducing strain due to the relative magnitudes of $\alpha\Delta T$ and $\frac{\Delta p}{H}$ in eq. (3) for reasonable values of sudden increases of ΔT and Δp. However it may be argued that, as demonstrated by previous studies on ground deformation in hydrothermal regions (e.g Hutnak et al., 2009; Fournier and Chardot, 2012), surface uplift due to the fluid migration from a deep input of hot and pressurized fluids is predominantly driven by the poro-elastic contribution for short timescales (as depending on the hydraulic diffusivity and the depth of the basis of the reservoir). In the present work we assume changes in Δp and ΔT to occur suddenly and uniformly over a specific volume at basis of the reservoir, that is the TPE, so that the model does not account for fluid migration and it is suited to estimate the contribution to the uplift increase observed in an hydrothermal region during a given time interval. In order to reproduce the temporal dependence of an unrest process, after the sudden Δp and ΔT establishement within the TPE

region, it might be necessary to model the progressive migration of the initial changes in temperature and pore pressure that could affect a wider region, starting from the inclusion considered here. For the aforementioned reasons, we expect that during unrest episodes also the subsidence following the peak of uplift may be mainly related to the decrease of Δp due to the fluid discharge from the TPE inclusion toward the hydrostatic aquifers above, while ΔT may be considered unchanged during this stage. The assessment of this hint is left for future developements of the present study.

6. CONCLUSIVE REMARKS

The main result of the present work is that unlike Mogi and Fialko sources, the TPE source here proposed allows for a large deviatoric stress promoting thrust fault mechanisms inside. Accordingly, the heterogeneity of focal mechanisms observed at Campi Flegrei as in other volcanic provinces supports the existence of a TPE source. Moreover, inverted-displacement results indicate that a TPE source can better model the surface deformation than other sources. As suggested by the case of the 1982-1984 unrest episode at Campi Flegrei a TPE source can be considered as part of a complex system of deformation sources where both hydrothermal and magmatic processes contribute to the observed displacement field.

Another major advantage of the TPE disk model over the Mogi one is that a large pore pressure change Δp may be easily and quickly accomplished through vertical motion of the magmatic volatiles exolved at lithostatic pressure by an underlying magma reservoir. Instead the pressure P of a dense and highly viscous magma presumably decreases faster while uprising according to a "magmastatic" gradient (at least). Thus within the same depth range, large Δp values are transferred much more easily and faster than similar ΔP values.

Further developments of this model could take into account the heterogeneity of the poro-elastic half-space, attempting at simulating the observed stratigraphy at Campi Flegrei or in other volcanic areas. We conclude remarking that such analytical or semi-analytical models as those we consider here are of fundamental importance when it comes: *i*) to calibrate and assess the validity of more complex numerical models; *ii*) to study sensitivities without having to re-grid, as may be necessary in numerical models; *iii*) to quantify driving parameters using fast models in inversion / data assimilation ; *iv*) to study forecasts and their range of uncertainties much easier than in numerical models because of the calculation speed.

7. Acknowledgements

Two anonymous reviewers are gratefully acknowledged for constructive comments and fruitful suggestions that helped in improving the revised version of the manuscript. We thank Elisa Trasatti for useful suggestions and Luca D'Auria for the catalog of focal mechanisms related to the 1982-1984 unrest episode at Campi Flegrei.

References

Amoruso, A., Crescentini, L., and Berrino, G. (2008). Simultaneous inversion of deformation and gravity changes in a horizontally layered half-space: evidences for magma intrusion during the 1982–1984 unrest at campi flegrei caldera (italy). *Earth and Planetary Science Letters*, 272(1-2):181–188.

Amoruso, A., Crescentini, L., and Sabbetta, I. (2014). Paired deformation sources of the campi flegrei caldera (italy) required by recent (19802010) deformation history. *Journal of Geophysical Research: Solid Earth*, 119(2):858–879.

Battaglia, M. (2017). dmodels: A software package for modeling volcanic deformation. In *EGU General Assembly Conference Abstracts*, volume 19, page 4203.

Battaglia, M., Troise, C., Obrizzo, F., Pingue, F., and Natale, G. D. (2006). Evidence for fluid migration as the source of deformation at campi flegrei caldera (italy). *Geophysical Research Letters*, 33(1).

Belardinelli, M., Bonafede, M., and Nespoli, M. (2019). Stress heterogeneities and failure mechanisms induced by temperature and pore-pressure increase in volcanic regions. *Earth and Planetary Science Letters*, 525:115765.

Berrino, G. (1994). Gravity changes induced by height-mass variations at the campi flegrei caldera. *Journal of Volcanology and Geothermal Research*, 61(3):293 – 309. International Conference on Active Volcanoes and Risk Mitigation.

Berrino, G., Corrado, G., Luongo, G., and Toro, B. (1984). Ground deformation and gravity changes accompanying the 1982 pozzuoli uplift. *Bulletin volcanologique*, 47(2):187–200.

Bonafede, M. and Ferrari, C. (2009). Analytical models of deformation and residual gravity changes due to a mogi source in a viscoelastic medium. *Tectonophysics*, 471(1-2):4–13.

Calò, M. and Tramelli, A. (2018). Anatomy of the campi flegrei caldera using enhanced seismic tomography models. *Scientific Reports*, 8(16254).

Carlino, S., Somma, R., Troise, C., and Natale, G. D. (2012). The geothermal exploration of campanian volcanoes: Historical review and future development. *Renewable and Sustainable Energy Reviews*, 16(1):1004 – 1030.

Chiarabba, C. and Moretti, M. (2006). An insight into the unrest phenomena at the campi flegrei caldera from vp and vp/vs tomography. *Terra Nova*, 18(6):373–379.

Chiodini, G., Vandemeulebrouck, J., Caliro, S., D'Auria, L., Martino, P. D., Mangiacapra, A., and Petrillo, Z. (2015). Evidence of thermal-driven processes triggering the 2005–2014 unrest at campi flegrei caldera. *Earth and Planetary Science Letters*, 414:58–67.

D'Auria, L., Giudicepietro, F., Aquino, I., Borriello, G., Del Gaudio, C., Lo Bascio, D., Martini, M., Ricciardi, G. P., Ricciolino, P., and Ricco, C. (2011). Repeated fluid-transfer episodes as a mechanism for the recent dynamics of campi flegrei caldera (19892010). *Journal of Geophysical Research: Solid Earth*, 116(B4).

D'Auria, L., Massa, B., Cristiano, E., Gaudio, C. D., Giudicepietro, F., Ricciardi, G., and Ricco, C. (2014). Retrieving the stress field within the campi flegrei caldera (southern italy) through an integrated geodetical and seismological approach. *Pure and Applied Geophysics*, 172(11):3247–3263.

De Natale, G., Troise, C., Mark, D., Mormone, A., Piochi, M., Vito, M. A. D., Isaia, R., Carlino, S., Barra, D., and Somma, R. (2016). The campi flegrei deep drilling project (cfddp): New insight on caldera structure, evolution and hazard implications for the naples area (southern italy). *Geochemistry, Geophysics, Geosystems*, 17(12):4836–4847.

De Vivo, B. (2006). *Volcanism in the Campania Plain: Vesuvius, Campi Flegrei and Ignimbrites*, volume 9. Elsevier.

Di Vito, M. A., Acocella, V., Aiello, G., Barra, D., Battaglia, M., Carandente, A., Gaudio, C. D., Vita, S. D., Ricciardi, G. P., Ricco, C., et al. (2016). Magma transfer at campi flegrei caldera (italy) before the 1538 ad eruption. *Scientific reports*, 6:32245.

Di Vito, M. A., Isaia, R., Orsi, G., Southon, J. D., Vita, S. D., d'Antonio, M., Pappalardo, L., and Piochi, M. (1999). Volcanism and deformation since 12,000 years at the campi flegrei caldera (italy). *Journal of Volcanology and Geothermal Research*, 91(2-4):221–246.

Dieterich, J. H. and Decker, R. W. (1975). Finite element modeling of surface deformation associated with volcanism. *Journal of Geophysical Research (1896-1977)*, 80(29):4094–4102.

Dvorak, J. J. and Berrino, G. (1991). Recent ground movement and seismic activity in campi flegrei, southern italy: Episodic growth of a resurgent dome. *Journal of Geophysical Research: Solid Earth*, 96(B2):2309–2323.

Ekstrom, G. (1994). Anomalous earthquakes on volcano ring-fault structures. *Earth and Planetary Science Letters*, 128(3):707 – 712.

Eshelby, J. D. (1957). The determination of the elastic field of an ellipsoidal inclusion, and related problems. *Proc. R. Soc. Lond. A*, 241(1226):376–396.

Feigl, K. L., Gasperi, J., Sigmundsson, F., and Rigo, A. (2000). Crustal deformation near hengill volcano, iceland 19931998: Coupling between magmatic activity and faulting inferred from elastic modeling of satellite radar interferograms. *Journal of Geophysical Research: Solid Earth*, 105(B11):25655–25670.

Fialko, Y., Khazan, Y., and Simons, M. (2001). Deformation due to a pressurized horizontal circular crack in an elastic half-space, with applications to volcano geodesy. *Geophysical Journal International*, 146(1):181–190.

Fournier, N. and Chardot, L. (2012). Understanding volcano hydrothermal unrest from geodetic observations: Insights from numerical modeling and application to white island volcano, new zealand. *Journal of Geophysical Research: Solid Earth*, 117(B11).

Frohlich, C. (2001). Display and quantitative assessment of distributions of earthquake focal mechanisms. *Geophysical Journal International*, 144(2):300–308.

Gaeta, F. S., Peluso, F., Arienzo, I., Castagnolo, D., Natale, G. D., Milano, G., Albanese, C., and Mita, D. G. (2003). A physical appraisal of a new aspect of bradyseism: The miniuplifts. *Journal of Geophysical Research: Solid Earth*, 108(B8).

Geertsma, J. et al. (1973). Land subsidence above compacting oil and gas reservoirs. *Journal of Petroleum technology*, 25(06):734–744.

Hill, D. P. (2006). Unrest in long valley caldera, california, 1978–2004. *Geological Society, London, Special Publications*, 269(1):1–24.

Hurvich, C. M. and Tsai, C.-L. (1989). Regression and time series model selection in small samples. *Biometrika*, 76(2):297–307.

Hutnak, M., Hurwitz, S., Ingebritsen, S., and Hsieh, P. (2009). Numerical models of caldera deformation: Effects of multiphase and multicomponent hydrothermal fluid flow. *Journal of Geophysical Research: Solid Earth*, 114(B4).

Jackson, J. D. (1999). Classical electrodynamics.

Judenherc, S. and Zollo, A. (2004). The bay of naples (southern italy): Constraints on the volcanic structures inferred from a dense seismic survey. *Journal of Geophysical Research: Solid Earth*, 109(B10).

Lima, A., Vivo, B. D., Spera, F. J., Bodnar, R. J., Milia, A., Nunziata, C., Belkin, H. E., and Cannatelli, C. (2009). Thermodynamic model for uplift and deflation episodes (bradyseism) associated with magmatic–hydrothermal activity at the campi flegrei (italy). *Earth-Science Reviews*, 97(1-4):44–58.

Macedonio, G., Giudicepietro, F., D'auria, L., and Martini, M. (2014). Sill intrusion as a source mechanism of unrest at volcanic calderas. *Journal of Geophysical Research: Solid Earth*, 119(5):3986–4000.

McTigue, D. F. (1986). Thermoelastic response of fluid-saturated porous rock. *Journal of Geophysical Research: Solid Earth*, 91(B9):9533–9542.

Mindlin, R. D. (1936). Force at a point in the interior of a semi-infinite solid. *Physics*, 7(5):195–202.

Mogi, K. (1958). Relations between the eruptions of various volcanoes and the deformations of the ground surfaces around them. *Earthq Res Inst*, 36:99–134.

Myklestad, N. O. (1942). *Two problems of thermal stress in the infinite solid*, volume 9. Cornell University.

Nettles, M. and Ekstrom, G. (1998). Faulting mechanism of anomalous earthquakes near brdarbunga volcano, iceland. *Journal of Geophysical Research: Solid Earth*, 103(B8):17973–17983.

Perkins, T., Gonzalez, J., et al. (1984). Changes in earth stresses around a wellbore caused by radially symmetrical pressure and temperature gradients. *Society of Petroleum Engineers Journal*, 24(02):129–140.

Perkins, T., Gonzalez, J., et al. (1985). The effect of thermoelastic stresses on injection well fracturing. *Society of Petroleum Engineers Journal*, 25(01):78–88.

Prejean, S., Ellsworth, W., Zoback, M., and Waldhauser, F. (2002). Fault structure and kinematics of the long valley caldera region, california, revealed by high-accuracy earthquake hypocenters and focal mechanism stress inversions. *Journal of Geophysical Research: Solid Earth*, 107(B12):ESE 9–1–ESE 9–19.

Rice, J. R. and Cleary, M. P. (1976). Some basic stress diffusion solutions for fluid-saturated elastic porous media with compressible constituents. *Reviews of Geophysics*, 14(2):227–241.

Rinaldi, A., Todesco, M., and Bonafede, M. (2010). Hydrothermal instability and ground displacement at the campi flegrei caldera. *Physics of the Earth and Planetary Interiors*, 178(3):155 – 161.

Robertson, R. M. and Kilburn, C. R. (2016). Deformation regime and long-term precursors to eruption at large calderas: Rabaul, papua new guinea. *Earth and Planetary Science Letters*, 438:86–94.

Sambridge, M. (1999). Geophysical inversion with a neighbourhood algorithmII. Appraising the ensemble. *Geophysical Journal International*, 138(3):727–746.

Sorey, M. L., Suemnicht, G. A., Sturchio, N. C., and Nordquist, G. A. (1991). New evidence on the hydrothermal system in long valley caldera, california, from wells, fluid sampling, electrical geophysics, and age determinations of hot-spring deposits. *Journal of Volcanology and Geothermal Research*, 48(3-4):229–263.

Tizzani, P., Battaglia, M., Castaldo, R., Pepe, A., Zeni, G., and Lanari, R. (2015). Magma and fluid migration at yellowstone caldera in the last three decades inferred from insar, leveling, and gravity measurements. *Journal of Geophysical Research: Solid Earth*, 120(4):2627–2647.

Todesco, M., Costa, A., Comastri, A., Colleoni, F., Spada, G., and Quareni, F. (2014). Vertical ground displacement at campi flegrei (italy) in the fifth century: Rapid subsidence driven by pore pressure drop. *Geophysical Research Letters*, 41(5):1471–1478.

Trasatti, E., Acocella, V., Di Vito, M. A., Del Gaudio, C., Weber, G., Aquino, I., Caliro, S., Chiodini, G., de Vita, S., Ricco, C., and Caricchi, L. (2019). Magma Degassing as a Source of Long-Term Seismicity at Volcanoes: The Ischia Island (Italy) Case. *Geophysical Research Letters*.

Trasatti, E., Bonafede, M., Ferrari, C., Giunchi, C., and Berrino, G. (2011). On deformation sources in volcanic areas: modeling the campi flegrei (italy) 1982–84 unrest. *Earth and Planetary Science Letters*, 306(3-4):175–185.

Trasatti, E., Polcari, M., Bonafede, M., and Stramondo, S. (2015). Geodetic constraints to the source mechanism of the 2011–2013 unrest at campi flegrei (italy) caldera. *Geophysical Research Letters*, 42(10):3847–3854.

Troise, C., Natale, G. D., Schiavone, R., Somma, R., and Moretti, R. (2018). The campi flegrei caldera unrest: Discriminating magma intrusions from hydrothermal effects and implications for possible evolution. *Earth-Science Reviews*.

Williams-Jones, G., Rymer, H., and Rothery, D. A. (2003). Gravity changes and passive so2 degassing at the masaya caldera complex, nicaragua. *Journal of Volcanology and Geothermal Research*, 123(1-2):137–160.

Yang, X.-M., Davis, P. M., and Dieterich, J. H. (1988). Deformation from inflation of a dipping finite prolate spheroid in an elastic half-space as a model for volcanic stressing. *Journal of Geophysical Research: Solid Earth*, 93(B5):4249–4257.

Zollo, A., Judenherc, S., Auger, E., D'Auria, L., Virieux, J., Capuano, P., Chiarabba, C., de Franco, R., Makris, J., Michelini, A., and Musacchio, G. (2003). Evidence for the buried rim of campi flegrei caldera from 3-d active seismic imaging. *Geophysical Research Letters*, 30(19).

Zollo, A., Maercklin, N., Vassallo, M., Iacono, D. D., Virieux, J., and Gasparini, P. (2008). Seismic reflections reveal a massive melt layer feeding campi flegrei caldera. *Geophysical Research Letters*, 35(12).